

Supplementary Information for

Untethered control of functional origami micro-robots with distributed actuation

Larissa S. Novelino, Qiji Ze, Shuai Wu, Glaucio H. Paulino, Ruike Zhao

Glaucio H. Paulino, Ruike Zhao

E-mail: paulino@gatech.edu or zhao.2885@osu.edu

This PDF file includes:

- Supplementary text
- Figs. S1 to S22
- Tables S1 to S2
- Legends for Movies S1 to S4
- SI References

Other supplementary materials for this manuscript include the following:

- Movies S1 to S4

Supporting Information Text

1. Kresling Pattern Geometry and Design

A. Geometry. In this paper, we engineer the Kresling pattern (1, 2) to obtain desired mechanical properties and precise actuation. From a geometry perspective, the Kresling pattern is nonrigid origami and presents two stable states per unit cell. That means that each unit cell cannot transition between those two stable states through folding of the hinges alone. Each unit cell is tessellated with triangulated panels of equal geometry, that is, same panel angle α and lengths a and b (Fig. S1). In terms of geometrical assemblage, it is composed of multiple unit cells N , with the same or distinct geometries, that behave independently from each other. In fact, because each unit cell has two stable states, we can have 2^N stable states.

The vertices of the triangles, when folded, all lie on the top and bottom polygon circumscribed circles. Those polygons twist in relation to each other, and the angle between them is the twisting angle (ψ). This angle varies from ψ_1 (deployed) to ψ_2 (folded) as the unit cell is folded, showing the coupling between rotation and axial displacement. The Kresling pattern is designed based on the height of the unit cell in the two stable states, number n of polygon edges, and corresponding edge lengths, b . From those parameters, we compute the design parameters of the crease pattern, that is panel length a and angle α , as provided in (3)

$$\alpha = \cos^{-1} \left(\frac{x_2(x_2 - \cot(\pi/n))}{\sqrt{((x_2^2 + 1)(H_0^2(x_2^2 + 1) + x_2^2 \csc(\pi/n)^2))}} \right) \quad [S1]$$

$$a = b \sqrt{H_0^2 + \frac{x_2^2 \csc(\pi/n)^2}{(x_2^2 + 1)}} \quad [S2]$$

$$c = b \frac{\sqrt{(H_0^2(x_2^2 + 1))^2 + x_2^3 \cot(\pi/n)(x_2 \cot(\pi/n) + 2) + x_2^2}}{(x_2^2 + 1)} \quad [S3]$$

where H_0 and H are the heights in the stable states [0] and [1], respectively, and

$$x_1 = 2 \sin(\pi/n) \frac{(\sin(\pi/n) \sqrt{(\cot(\pi/n)^2 \csc(\pi/n)^2 - (H^2 - H_0^2)^2) - \cos(\pi/n)}}{1 + H^2 - H_0^2 + (1 - H^2 + H_0^2) \cos(2\pi/n)} \quad [S4]$$

$$x_2 = 2 \sin(\pi/n) \frac{(\sin(\pi/n) \sqrt{(\cot(\pi/n)^2 \csc(\pi/n)^2 - (H^2 - H_0^2)^2) - \cos(\pi/n)}}{1 - H^2 + H_0^2 + (1 + H^2 - H_0^2) \cos(2\pi/n)} \quad [S5]$$

The twisting angles in the two stable configurations are computed as

$$\psi_1 = 2 \tan^{-1} x_1, \quad \psi_0 = 2 \tan^{-1} x_0 \quad [S6]$$

When the twisting angle between bottom and top vertices of a valley fold is equal to 180° , that is $\psi_0 = \pi - 2\pi/n$, the valley folds meet at the center, making this a critical design. If $\psi_0 > \pi - 2\pi/n$, the pattern will experience contact among its panels and will not be able to reach the folded stable state. This angle restriction results in a design constraint on the choice of the height difference between stable states (3),

$$|H^2 - H_0^2| \leq \cot^2(\pi/n) \quad [S7]$$

In this paper, because we work with compact assemblies that have large changes in geometry, we opt for flat-foldable designs, that is, we design the unit cells to have zero height at the folded state ($H_0 = 0$). In addition, all the designs are based on hexagons ($n = 6$) with sides length $b = 13$ mm, resulting on height restriction of $H_{crit} = 22.52$ mm. Respecting this design constraint, we investigate unit cells with $H = 15.6$ mm, 16.9 mm, 18.2 mm, and 20.8 mm (see Table S1). For each unit cell, we define the folded and deployed stable states as state [0] and state [1], respectively (Fig. S1A).

B. Mechanics. Geometrically, the Kresling pattern always presents bistability, with an energy barrier correlated to the height of the unit cell. However, this statement is only valid under the assumption of zero stiffness hinges. In reality, the crease lines store energy as we fold the pattern, making the existence of bistability dependent on the material properties of both hinges and panels. To guide our design, we simulate the unit cells with distinct heights (Fig. S2) using the MERLIN software (4). This software uses a nonlinear formulation combined with the modified generalized displacement control method (5), which allows tracking of the complete equilibrium path, even for structures displaying snap-type behavior, as is the case of the Kresling pattern. The MERLIN software uses a reduced order model (6, 7) that considers the crease lines as bars with rotational springs along them. For non-triangular (quadrilateral) panels, this model adds an extra bar along the panels' shortest diagonals to avoid mechanisms and to approximate the bending of the panels. However, because the Kresling pattern is already tessellated by triangles, the simulation will not consider any bending of the panels and consider that all the deformation occurs either by the folding of the hinges or stretching of the crease lines and panels. The reduced order model provides information on the global behavior of the unit cell and how the geometry is correlated with the energy barrier between stable states (4).

2. Samples Fabrication

We fabricate each unit cell of the Kresling pattern by perforating and cutting the pattern on Tant origami paper (0.1mm thick) with the PLS4.75 laser cutting system (Universal laser systems). The Kresling pattern is modified to a flower-like shape (Fig. S1B) to accommodate the cuts along the mountain folds. Those cuts avoid kinks in the mountain folds, creating samples with similar response on multiple folding cycles (8). After the pattern is folded, we use 3M Scotch double sided tape to attach the top and bottom polygons (Fig. S1C). These polygons are made of 160g/m Canson Mi-Teintes paper (0.2 mm thick), a thicker paper meant to provide stiffness and avoid bending of the polygons.

To the top of each unit cell, we attach the magnetized plate using Sil-Poxy silicone adhesive. We fabricate the magnetized plates by first mixing Ecoflex 00-30 silicone rubber and NdFeB particles into a homogeneous mixture with 30% NdFeB volume. This mixture is poured into a circular 3D-printed mold with 22mm of diameter and 3mm of depth and cured for one hour at 60°C. Next, we magnetize the plates using a magnetizer with an 1.5T impulse magnetic field. In Table S2, we provide the magnetization directions of the magnetic plates at the folded state with respect to the x axis and the geometries of the unit cells for the Kresling assembly presented in the main text.

We investigate the variability of the mechanical properties over multiple compression cycles. In Fig. S3, we show the force-displacement response of a design 3 unit cell (see Table S1) up to its 500th folding cycle. We observed that the mechanical response stabilizes around the cycle 300. Thus, for consistent results, all the samples were folded and deployed up to 300 times prior to performing the magnetic actuation and mechanical tests reported in this work.

3. Mechanical Test

We test the mechanical properties of the Kresling unit cells under compression using a customized testing bed (Fig. S4) that was previously reported in (9). The setup consists of a metallic frame that integrates two steel plates. One plate is fixed and is connected to a 50N capacity load cell (RSP1, Loadstar Sensors) with accuracy to 0.02% full scale. The other plate is movable and is controlled by a stepper motor (STP-MTR-23079, SureStep). The testing bed has a safety mechanism that limits the distance between the two plates to be no smaller than 15mm, which is about the size of our samples. To overcome this size limitation, we add a 3D-printed sample holder to the setup.

From the experiments, we observe that the stable states of the samples differ from the geometric folded stable state. In reality, the folded stable state is not equivalent to the flat-foldable state (that is, $H_0 > 0$). Similarly, the rotational angles $\delta\theta$ are also different from those geometrically computed $\Delta\psi$ and reported in Table S1. This difference comes from the fact that the fabricated samples have panels with thickness and hinges with stiffness, while the geometric model assumes panels with zero thickness and hinges with zero stiffness.

A. Setup #1: Folding of the Unit Cell. For each unit cell design in Table S1, we test five samples under compression. For the tests, we attach one end of the unit cell to the sample holder, while leaving the other end completely free (Fig. S4). The free end is compressed against the fixed plate. To reduce the friction between the sample and the fixed plate, we lubricate the fixed plate before each test. Note that because the sample has no physical connection to the fixed plate, once the sample snaps, the free end loses contact with the load cell (see snapshots in Fig. S3). This results in the region with zero load in the force-displacement curves. Once the free end reaches the load cell again, we see the load increasing (Fig. 3A).

B. Setup #2: Folding and Deployment of the Unit Cell. Because we need to measure the required forces to both fold (compress) and deploy (pull) the unit cell, we modified the boundary conditions of the testing setup. For deployment, we need to constrain both ends of the unit cell, while allowing for rotation of the end in contact with the fixed plate. Thus, we use a wire to attach the crease pattern to a pre-lubricated acrylic plate (Fig. S5A). In the acrylic plate, we laser cut a hole and a slot, allowing for the wire to pass through the plate and to be folded into the slot. This wire connection is enough to constraint the unit cell to the plate, while allowing for it to freely rotate. Once the attachment is done, we fold the unit cell, as described previously (Fig. S1C). Next, we attach the acrylic plate to the testing bed fixed plate and attach the bottom of the unit cell to the sample holder (Fig. S5B,C). We first compress (fold) each unit cell from the deployed to the flat-folded state. Because both ends of the unit cell are constrained, the sample will not lose contact with the load cell. Thus, we obtain the entire equilibrium path between the stable states (Fig. S6) in which we observe a change in the direction of the axial load (from compression to tension). Once the unit cell reaches the stable state [0], the load changes direction again (from tension to compression) and the unit cell is compressed until it reaches the flat-folded state. After reaching the flat-folded state, we start the deployment of the unit cell. At first, the unit cell deploys without any force being applied (i.e., the unit cell experiences unloading). After a stable state is reached, the unit cell starts to experience tension. Similarly to the folding process, we capture the entire equilibrium path and we observe a change in the direction of force (from tension to compression). Once the unit cell reaches another stable, further deployment is only possible under tension (Fig. S6).

C. Mechanical Properties of the Four-Cell Kresling Pattern. We investigate the mechanical tunability of the four-cell Kresling pattern (Fig. 3D,E) by axial compression of the assembly at all sixteen stable states. The assembly is composed of unit cells with designs 1 to 4 (top to bottom) presented in Table S1. However, because the folded unit cells (state [0]) are not completely flat-folded during the experiments, we decided to remove them for a better quantification of the stiffness of the assembly in each state. Thus, we test only the unit cells that are deployed. For example, the quantification of the stiffness of the stable state [1001] involves testing the assembly using only the unit cells with design 1 and 4.

For each one of the sixteen stable states, we test the same assembly sample under compression three times using the experiment setup #1 described in SI Section 3A. That is, the assembly has one end attached to the sample holder, and the other end is free. The legend in Fig. S7 refers to the stable state of the unit cells (from bottom to top), and it is in this figure that we show the averaged force-displacement curves for all three tests in each of the stable states. By comparing those curves, we observe a dramatic change in the mechanical behavior between some of the stable states, showing that we can use our actuation method to tailor the mechanical properties of a Kresling metamaterial.

From the force-displacement curves, we obtain the stiffness K . This stiffness is defined as the slope of the first linear region of the force-displacement curves. In Fig. 3E, we compare theoretical values of the equivalent modulus for each state with the measured values. The theoretical values are obtained from the simplification of the four-cell assembly to a system of springs in series, where the stiffness of each spring corresponds to the stiffness of each unit cell that is obtained from the compression test. Thus, we compute the theoretical stiffness K_{eq} as

$$\frac{1}{K_{eq}} = \sum_{i=1}^N \frac{1}{K_i} \quad [S8]$$

where K_i is the stiffness of each spring (i.e., unit cell) i in the deployed state and N is the number of deployed unit cells. Because the values of K_i are obtained experimentally, in Fig. 3E, we provide the theoretical values computed with the averaged (columns), maximum and minimum (error bars) stiffness values. The averaged measured values for single unit cells are $K_1 = 0.25$ N/mm, $K_2 = 0.39$ N/mm, $K_3 = 0.59$ N/mm, and $K_4 = 1.26$ N/mm.

In Fig. S8, we provide a comparison of the modulus E of each state, which is defined as the slope of the first linear region of the stress-strain (σ - ϵ) curves, being expressed as

$$E = \frac{\sigma}{\epsilon} = \frac{F}{A} \frac{H}{\Delta H} \quad [S9]$$

where F is the measured force, A is the area of the unit cell polygon, ΔH is the applied displacement, and H is the sum of the heights of the deployed unit cells. The averaged measured values for single unit cells are $E_1 = 0.86 \times 10^{-2}$ N/mm², $E_2 = 1.4 \times 10^{-2}$ N/mm², $E_3 = 2.4 \times 10^{-2}$ N/mm², and $E_4 = 5.9 \times 10^{-2}$ N/mm².

4. Magnetic Actuation Experiment

A. Electromagnetic Coil. The Kresling patterns with magnetic plates are actuated within a customized electromagnetic coil system, which can generate a two-dimensional (2D) uniform magnetic field (Fig. S9). Two sets of standard Helmholtz coils are configured perpendicularly to each other in the xy -plane. The in-plane magnetic field direction and intensity can be accurately controlled by the current in the coils. The coils can generate 2.7 mT/A and 3.3 mT/A uniform magnetic fields with 60mm and 80mm spacing for the x and y axes, respectively.

B. Uniformity of Magnetic Field. In order to quantitatively study the magnetic field distribution, finite element analysis is performed to show that the magnetic field generated by the two pairs of Helmholtz coils are sufficiently uniform in both axial direction and perpendicular direction. The 2D Helmholtz coil used for magnetic actuation is shown in Fig. S9. Defining the central point in the 2D coils as the origin of the xyz coordinate system, the simulation results of the magnetic field distribution with 10A current in the coils are shown in Fig. S10. Here we define the uniformity of the magnetic field in any axis as $1 - (B_{max} - B_{min})/B_{center}$, where B_{max} , B_{min} , and B_{center} are the maximum, minimum, and central fields within the defined range, respectively.

The magnetic field used to actuate the origami is in the xy plane. The distances between two coils in the x and y axes are 80mm and 60mm, respectively. The field in x direction is denoted by B_x , which is generated by a pair of coils along the x axis. The field in y direction is denoted by B_y , which is generated by a pair of coils along the y axis. The uniformities of B_x along the x axis and z -axis are 98.8% and 99.9%, respectively, for the working space between -40 mm and 40 mm. The uniformities of B_y along the y -axis and z axis are 99.0% and 99.8%, respectively, for the working space between -30 mm and 30 mm. The simulation results indicate that the magnetic field generated by the two pairs of Helmholtz coils are sufficiently uniform in all directions.

The origami assemblies in this paper are more sensitive to the uniformity of the magnetic field along the z axis, especially when the number of the unit cells is large. The maximum height of the origami assembly in this paper is about 85 mm as shown in Fig. 2 and Fig. S10. For this height, the uniformity of the magnetic field can be larger than 98.5% in both xy plane and z axis. Even when the height increases to 120 mm, the uniformity can still reach 93.2%, which is sufficiently high for this application.

C. Magnetic Actuation. All Kresling unit cells and multicell assemblies are tested in the 2D electromagnetic coils. The Kresling samples are attached to an acrylic support (Fig. S9), so that only the bottom polygon is constrained against any type of displacement, and the other end is completely free. All magnetic plates are placed parallel with the xy plane of the coils. The induced magnetic torque can fold and deploy the patterns along the z axis. Then, a specific direction of the magnetic field is set, and the amplitude increases from 0 mT to 30 mT at a rate of 1 mT/s. When the Kresling patterns change states, the corresponding magnetic field is recorded. This is the minimum required magnetic field to actuate the Kresling pattern in this

specific direction. Then, we change the magnetic field direction and repeat the same procedure. A step of 5° is used to scan the xy -plane from 0° to 360° . We fit the recorded magnetic field direction and amplitude data using the Fourier series and plot the corresponding experimental contours of magnetic actuation (Fig. 1C and E, Fig. 2D, Fig. 3C, Fig. S11C, Fig. S12, and Fig. S13).

5. Distributed Actuation

A. Unit cell Actuation. Each Kresling pattern can be locally actuated (i.e., folded and deployed) under a magnetic field \mathbf{B} . In Fig. 1A-C and Fig. S11, we show the actuation process and required actuation parameters (θ_B and B) for the folding and deployment a design 3 (Table S1) unit cell, respectively. We define $Tr+$ and $Tr-$ as the required torques to fold and deploy, respectively, the unit cells. Because of rotation and displacement coupling of the Kresling pattern (SI Section 6), the required torques are obtained from the uniaxial test with displacement control described in SI Section 3B.

B. Assembly Actuation. From the individual actuation allowed by the attached magnetic plates, a local torque can be induced in each unit cell. In Fig. S12, we show the contour plots with the required actuation parameters (B and θ_B) for the two-cell Kresling assembly (Fig. 1D) from, and to, any stable state. Following, we discuss the actuation from the [00] to the states [01], [10], and [11] for the assembly shown in Fig. 1D:

- **From Global State [00] to [10]:** The change of state occurs under a magnetic field with intensity $B = 20$ mT and direction $\theta_B = 120^\circ$. The magnetic field induces a counterclockwise magnetic torque, which is enough to deploy the bottom unit cell, but not the top unit. Thus, only the bottom unit cell deploys, rotating by $\delta\theta_1$. The top unit cell remains in the folded configuration, rotating by $\delta\theta_1$ as a rigid body with the bottom unit cell.
- **From Global State [00] to [01]:** The change of state occurs under a magnetic field with intensity $B = 20$ mT and direction $\theta_B = 240^\circ$. In the bottom unit cell, the magnetic field induces a clockwise magnetic torque that is opposite to the rotation direction for deployment, preventing the state change ($\delta\theta_1 = 0$). While, in the top unit cell, the magnetic field induces a counterclockwise torque larger than the required torque (i.e., $T < Tr-$), leading to the unit cell deployment with a rotation $\delta\theta_2$.
- **From Global State [00] to [11]:** The change of state occurs under a magnetic field with intensity $B = 20$ mT and direction $\theta_B = 180^\circ$. In both bottom and top unit cells, the magnetic field induces a counterclockwise torque larger than the required torque (i.e., $T < Tr-$). Thus, the bottom unit cell rotates by $\delta\theta_1$ and the top unit cell rotates by $\delta\theta_1 + \delta\theta_2$.

6. Rotation and Displacement Coupling

Because the Kresling pattern displays a coupling between compression and torsion, we can obtain the required torque to fold the unit cells from the uniaxial compression test. Thus, we use a compression test setup to measure the force needed to transition between the two stable states of the pattern (Fig. 3A). From the measured results, we obtain the stored energy. The derivative of the stored energy with respect to the rotation angle variation $\delta\theta$ results on the torque ($Tr+$) required to fold the unit cells. Thus, we express the stored energy as a function of $\delta\theta$, instead of ΔH (Fig. S14). With the torque, we compute the parameters (B and θ_B) needed to actuate each one of the unit cell designs (Table S1), which are provided in Fig. S13.

Although the Kresling pattern has a coupling between rotation and axial displacement, the relationship between the two is not available from kinematic equations. Because the Kresling pattern is a nonrigid origami, we only have a geometrical relationship between height and rotation angle $\delta\theta$ at the stable states. Thus, we approximate this relationship from the simulation of each unit cell under axial load using the MERLIN software (4). From the displacement history of the nodal coordinates, we obtain both the axial and rotational displacements of the unit cell. We approximate this data by a polynomial function and use this function to plot the stored energy as a function of the rotation angle.

7. Material Characterization

A. Mechanical Properties. To measure the stiffness of the hinges, we test samples with a primary hinge manufactured with the same process as the valley folds of the Kresling unit cell samples. That is, the hinge is cut with a dashed line pattern and is folded and deployed for 300 cycles. Parallel to the primary hinge, we add secondary hinges that are made weaker than the primary one, making the stiffness at those hinges close to zero.

Each end of the sample is attached to an acrylic plate. Those plates have a slit cut, allowing for the edges of the sample to pass through it and be folded and taped on the other side. The acrylic plates are assembled to the test bed shown in Fig. S4, such that one plate is attached to the sample holder and the other to the fixed plate (Fig. S15). From the experiment, we measure the displacement d and force F , and with this information, we calculate the bending moment M_b and the change in folding angle $\delta\phi$ as

$$M_b = F\delta\ell, \quad \delta\phi = 2 \sin^{-1}(d_0/2b) - 2 \sin^{-1}(\delta d/2b) \quad [\text{S10}]$$

where $\delta\ell$ is the vertical distance between the edges and the hinge, $b = 13$ mm is the panel size, $d_0 = 21$ mm is the initial opening of the hinge, and $\delta d = d_0 - d$ (Fig. S15B). From the slope of the bending moment versus folding angle curves, we obtain the rotational stiffness of the hinges. This value is divided by the length of the hinge, that is 50 mm, resulting on an average stiffness of $k_f = 2.4 \times 10^{-3} \text{ N}\cdot\text{mm}(\text{rad}\cdot\text{mm})^{-1}$.

B. Magnetic Properties. The magnetic properties of the magnetic material for the plates are measured on a Vibrating Sample Magnetometer (VSM, 7400A series, Lake Shore Cryotronics, Inc., Chicago, IL, USA). The magnetic moments of the material under external magnetic field (B) from -1.5 T to 1.5 T are scanned and recorded. The corresponding magnetic moment densities (M) are calculated from the magnetic moments by dividing by the sample volume. From the measured M-B curve in Fig. S16, the remanent magnetic moment density (M_r) is 177.39 kA/m and will be used as the magnetization intensity M for analyzing the magnetic actuation performance in the next section.

8. Analytical Calculation for Magnetic Actuation

Under a uniform magnetic field, the magnetic torque (T) will be induced to align the magnetization direction of the magnetic material to the external magnetic field and is calculated as

$$T = BMV \sin(\theta_M - \theta_B) \quad [S11]$$

where V is the volume of the magnetic plate, B is the magnetic field intensity, θ_M and θ_B are the directions of the magnetization and the external magnetic field, respectively. With the folding process of a Kresling pattern as an example in Fig. 1A, the Kresling pattern will rotate clockwise. The angles of $\delta\theta_s$ and $\delta\theta$ are defined as the angle difference between two stable states and the real-time rotation angle during the actuation process, respectively. The Kresling pattern can be changed to state [0] (folded) when the magnetic torque (T) is larger than the required torque (Tr_+) at any angle $\delta\theta$ (Fig. 1B). In the analytical calculations, 0.1° is chosen as the angle step.

The state of the Kresling pattern under a specific magnetic field direction and amplitude will be determined as in the flowchart shown in Fig. S17, and the states of the Kresling patterns under different magnetic field directions can be predicted numerically with the same flow. The analytical results shown in Fig. 1C, Fig. S11C, and Fig. S13 display good agreement with the experimental results.

9. LED Circuit

A. Fabrication. In the modified crease pattern (Fig. 4B), we glue a layer of foam to the unit cell, followed by a layer of copper tape (0.1 mm thick). Next, we connect the copper tape to a copper wire and finally fold and assembly the unit cells and magnetized plates.

B. Schmitt trigger circuit. Schmitt trigger is a frequently used analog-to-digital converter circuit, which exhibits the same bistable characteristic as the designed Kresling patterns. The applied magnetic torque can be used to change the states of the Kresling pattern between state [0] and state [1]. In correspondence, the input voltage of the Schmitt trigger can be used to change its output between U_H and $-U_H$, which are regulated by reverse connected Zener diodes. Therefore, the applied magnetic torque can be considered as the input of the “origami Schmitt trigger”. Fig. S18A shows the typical hysteresis loop of the “origami Schmitt trigger”. To show the similar characterization between Schmitt trigger and a Kresling pattern unit cell, a demonstration of two LEDs with different colors showing the different states is designed and its comprehensive circuit is shown in Fig. S18B. When the applied magnetic torque is larger than the positive required torque of the specific Kresling pattern, the output voltage is U_H , which can be used to drive controllable switches. The green LED is short-circuited by Switch 1 and the blue LED is turned on to indicate the state [0] of the unit cell. In contrast, when the applied magnetic torque is smaller than the negative required torque, the output voltage will snap to $-U_H$. In this case, the controllable switch will be opened. The green LED is turned on to indicate state [1] of the unit cell. The Zener diodes D_1 and D_2 with Zener voltage of U_H are used to regulate the output voltage U_0 . The reference input T_{ref} and resistances R_1 , R_2 are used to reflect the mechanical properties of the Kresling pattern. As we have already measured the positive and negative required torque of the specific Kresling pattern, T_{ref} and the ratio between R_1 and R_2 can be calculated as

$$T_{\text{ref}} = \frac{U_H(Tr_+ + Tr_-)}{2U_H + Tr_+ - Tr_-}, \quad \frac{R_1}{R_2} = \frac{Tr_+ - Tr_-}{2U_H} \quad [S12]$$

C. LED demonstration for Kresling pattern assembly. For the LED circuit in Fig. 4, we use designs 1,3 and 4 (green, yellow and red unit cells, respectively) to create the logic circuit. Fig. S18(C) shows the schematic of the LED demonstration for Kresling assembly. As the three unit cells have different mechanical properties, the corresponding “Origami Schmitt trigger” has different input references and resistance ratios. And their input torques can be calculated as

$$T_1 = T_{M1} + T_{M2} + T_{M3}, \quad T_2 = T_{M2} + T_{M3}, \quad T_3 = T_{M3} \quad [S13]$$

where T_{M1} , T_{M2} , and T_{M3} are the applied magnetic torques of each unit cell.

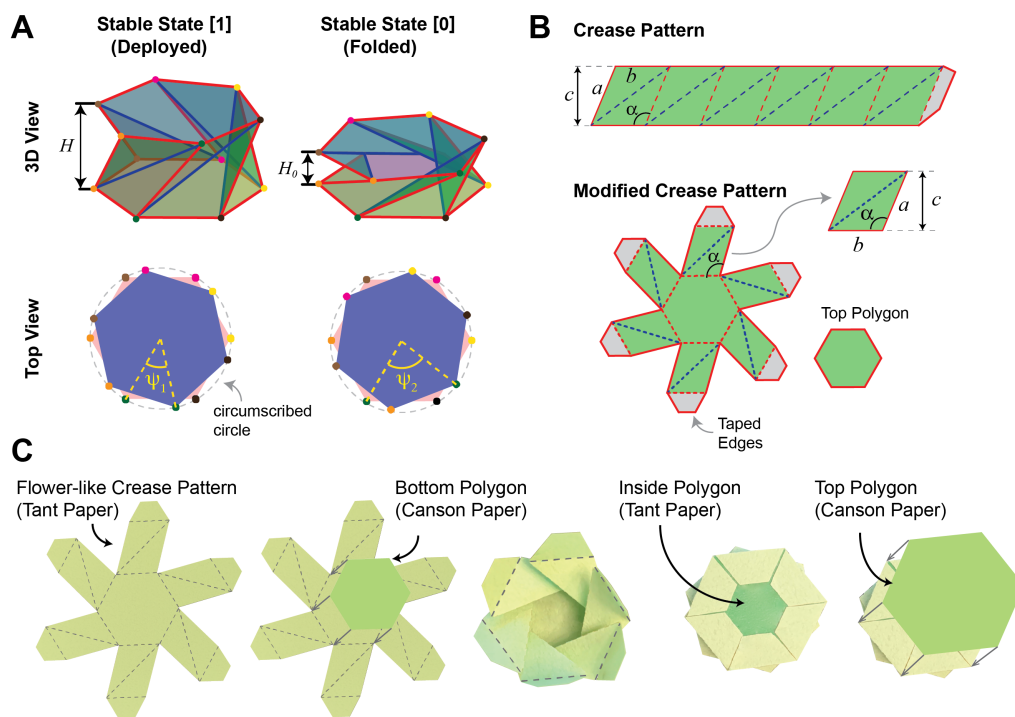


Fig. S1. Kresling pattern (A) geometry, (B) crease pattern, and (C) fabrication steps.

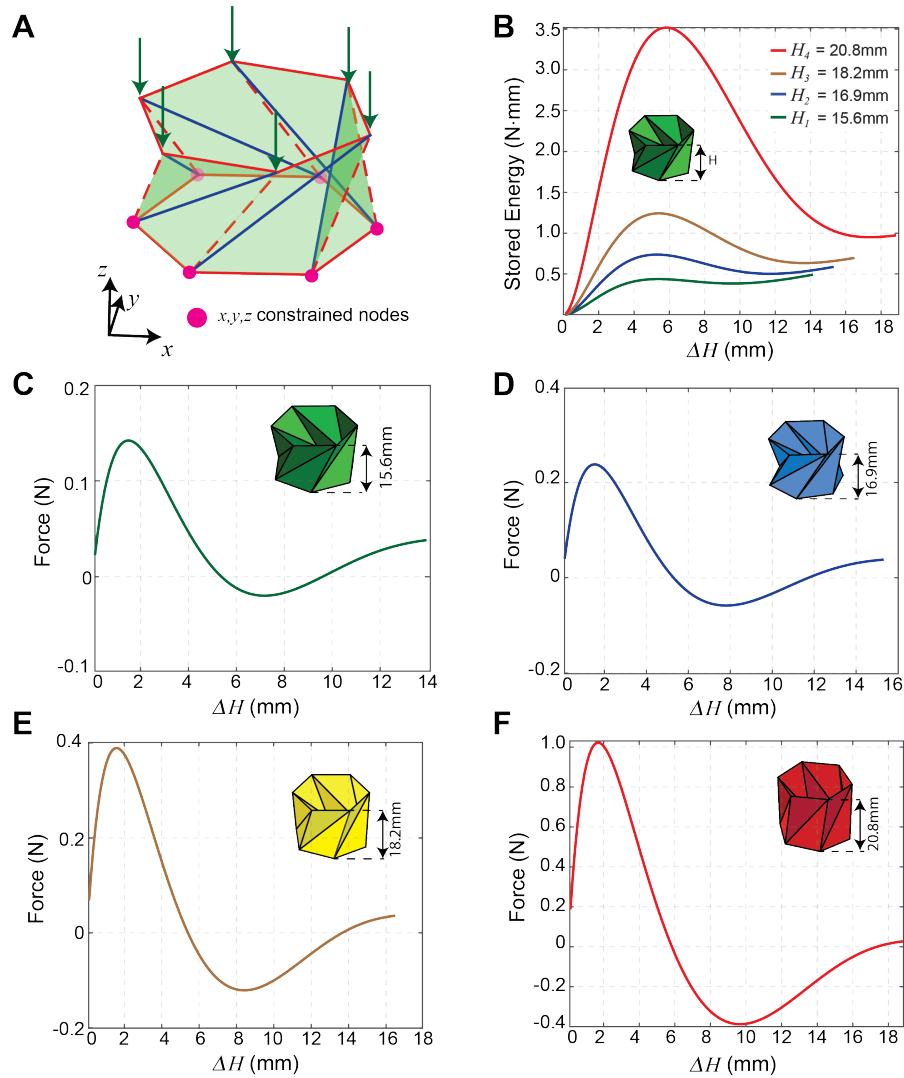


Fig. S2. Simulation of the Kresling unit cell used to guide the geometric design. (A) Bar-and-hinge model representing the unit cell. Valley folds (blue lines) are modeled by bars with area $A \approx t \times b$, where the paper thickness $t = 0.1$ mm and $b = 13$ mm, and rotational springs with stiffness $k_f = 2.4 \times 10^{-3}$ N·mm(rad·mm) $^{-1}$. Mountain folds with slit cuts (dashed lines) are modeled as bars with area $A_{slit} \approx 0.5A$ and rotational springs with stiffness $k_{slit} \approx 0.01k_f$. Arrows represent the direction of applied displacement $0.9H_i$ ($i = 1..4$). (B) Stored energy vs. displacement curve. Force-displacement curves for (C) Design 1 ($H_1 = 15.6$ mm), (D) Design 2 ($H_2 = 16.9$ mm), (E) Design 3 ($H_3 = 18.2$ mm), and (F) Design 4 ($H_4 = 20.8$ mm).

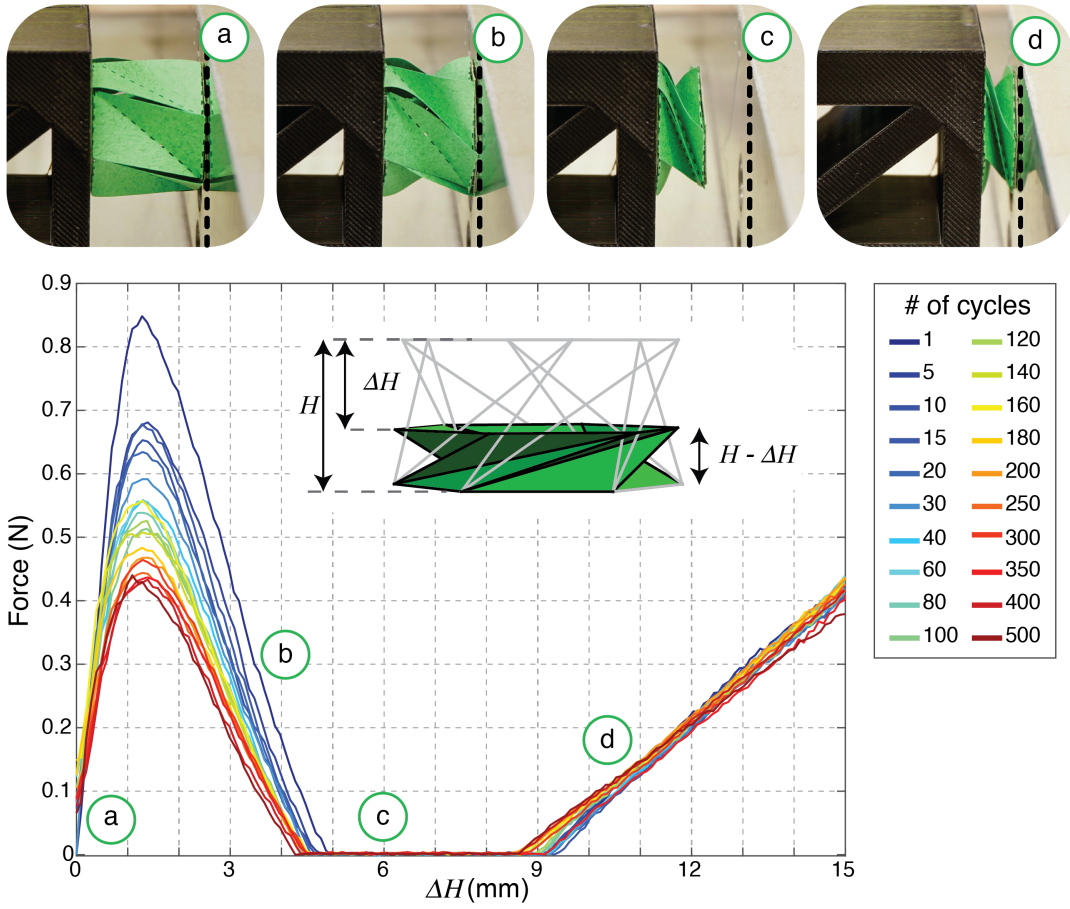


Fig. S3. Kresling pattern (Design 3, $H = 18.2$ mm) responses up to 500 compression cycles and snapshots of the experiment. Points a, b, and d are contact points, while point c is a non-contact point. Note that once the unit cell snaps, it loses contact with the load cell (e.g. point c), resulting on null forces until the contact is restored (e.g. point d).

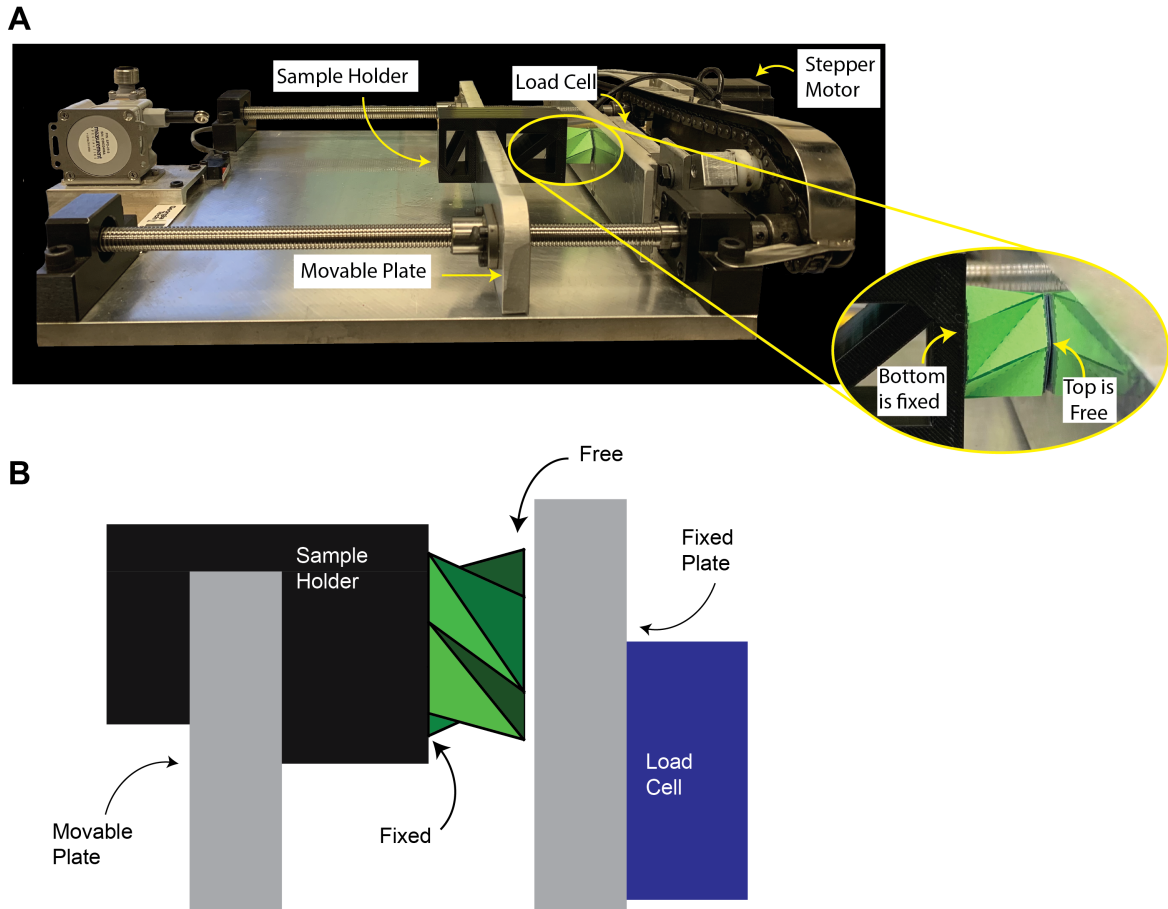


Fig. S4. Compression test (setup #1). (A) Compression test bed and (B) Schematic of the test with fixed-free boundary conditions.

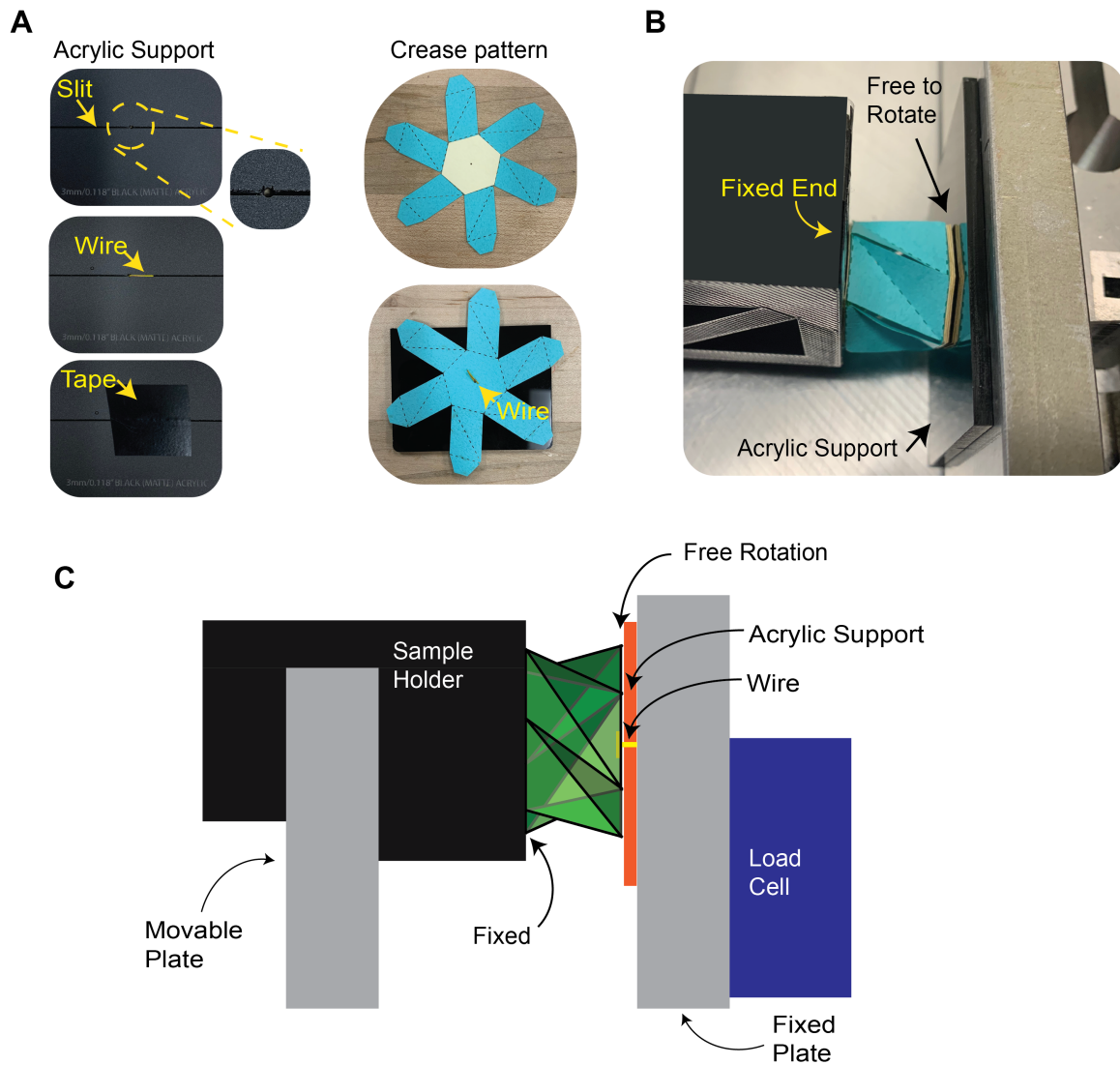


Fig. S5. Compression and Tension test (setup #2). (A) Modified sample with a wire connection to an acrylic plate. (B) Sample assembled in the test bed. The sample is directly attached to the sample holder and the acrylic support to the fixed plate. (C) Schematic of the test setup.

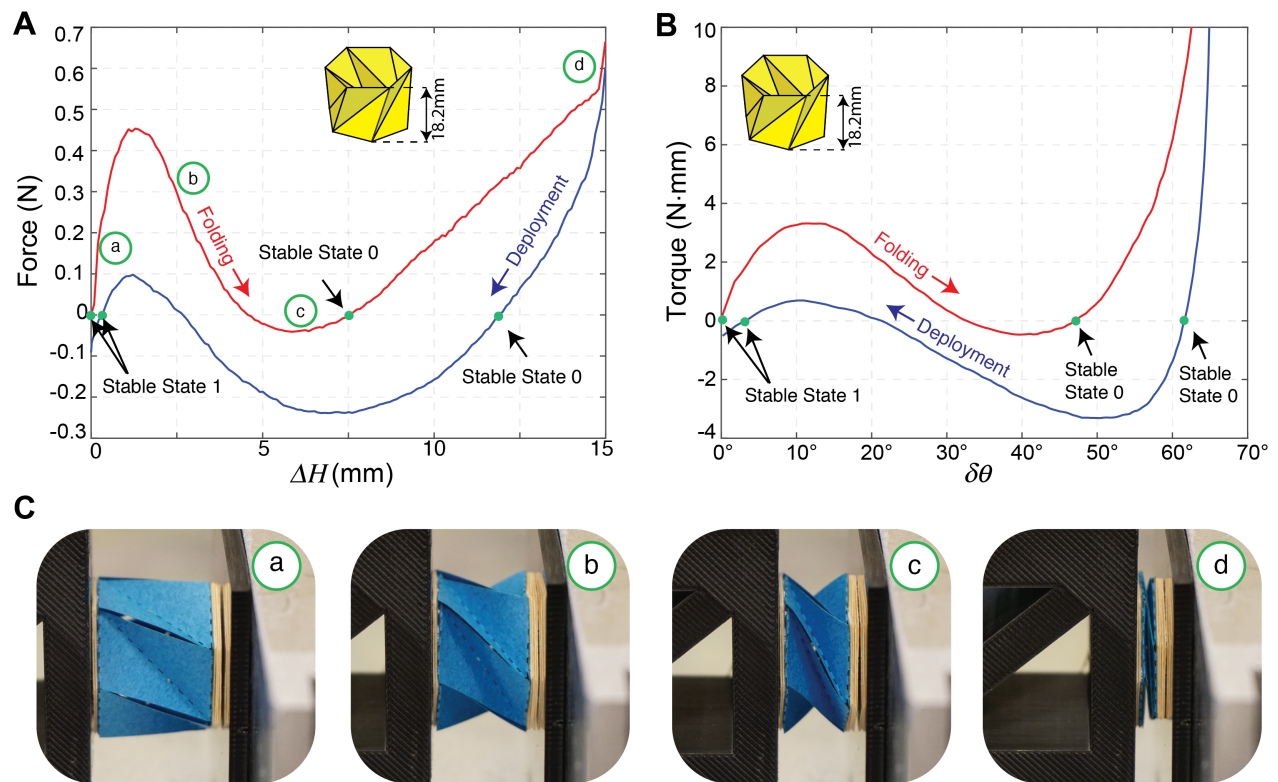


Fig. S6. (A) Force-displacement curve obtained from the compression/tension test (setup #2) of the Design 3 unit cell. (B) Torque-rotation curve obtained from the derivation of the stored energy. (C) Snapshots of the experiment. Note that the left side of the sample is fixed to the sample holder and the right side uses a wire connection that constrains the unit cell while allowing for free rotation. The constraints at both ends permit the measurement of the entire equilibrium path. Contact at the right-hand-side of the setup is maintained at all times (points a, b, c, d).

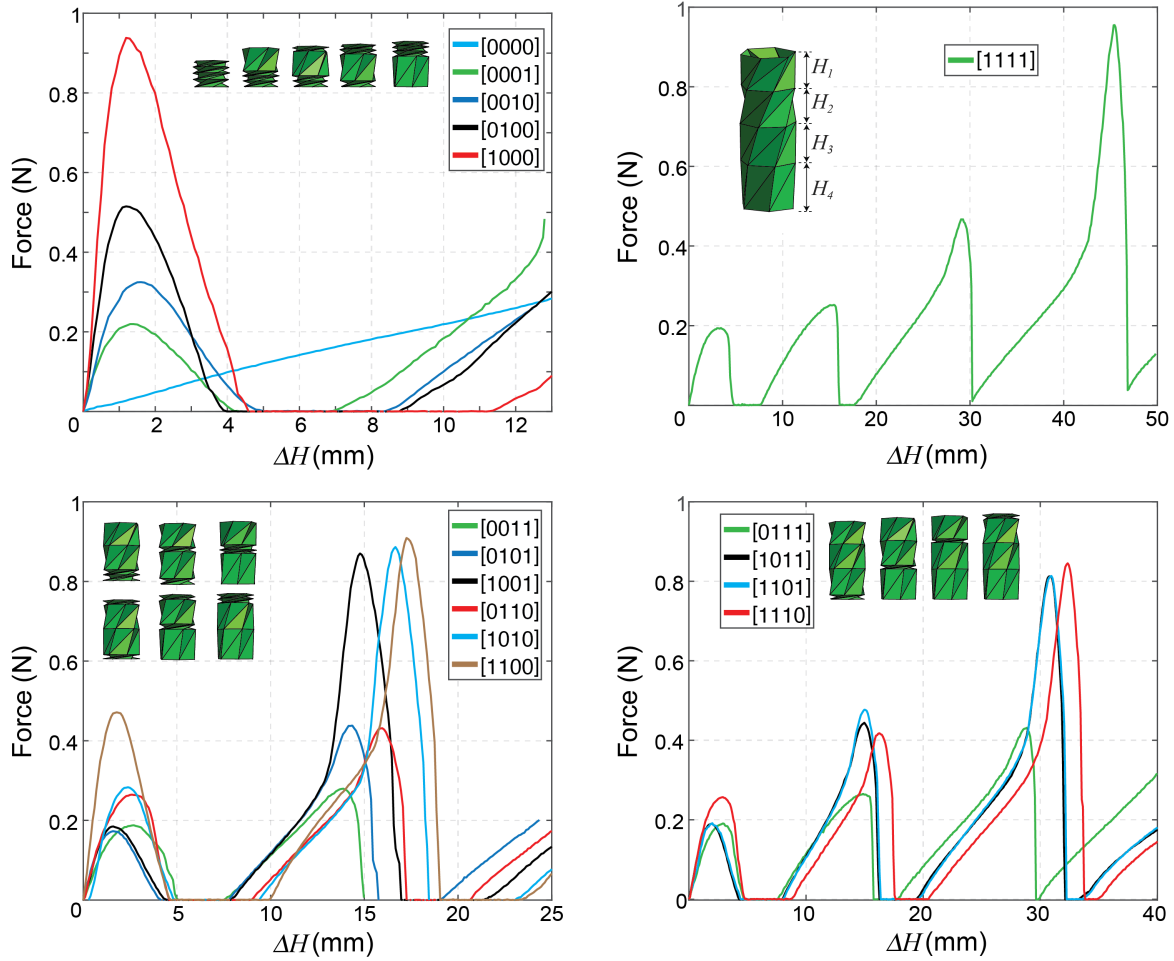


Fig. S7. Average force-displacement curves of the sixteen stable states of the four-cell Kresling assembly, where $H_1 = 15.6$ mm, $H_2 = 16.9$ mm, $H_3 = 18.2$ mm, and $H_4 = 20.8$ mm. For this test, we use setup #1 (Fig. S4). Legend refers to the state of each unit cell (bottom to top).

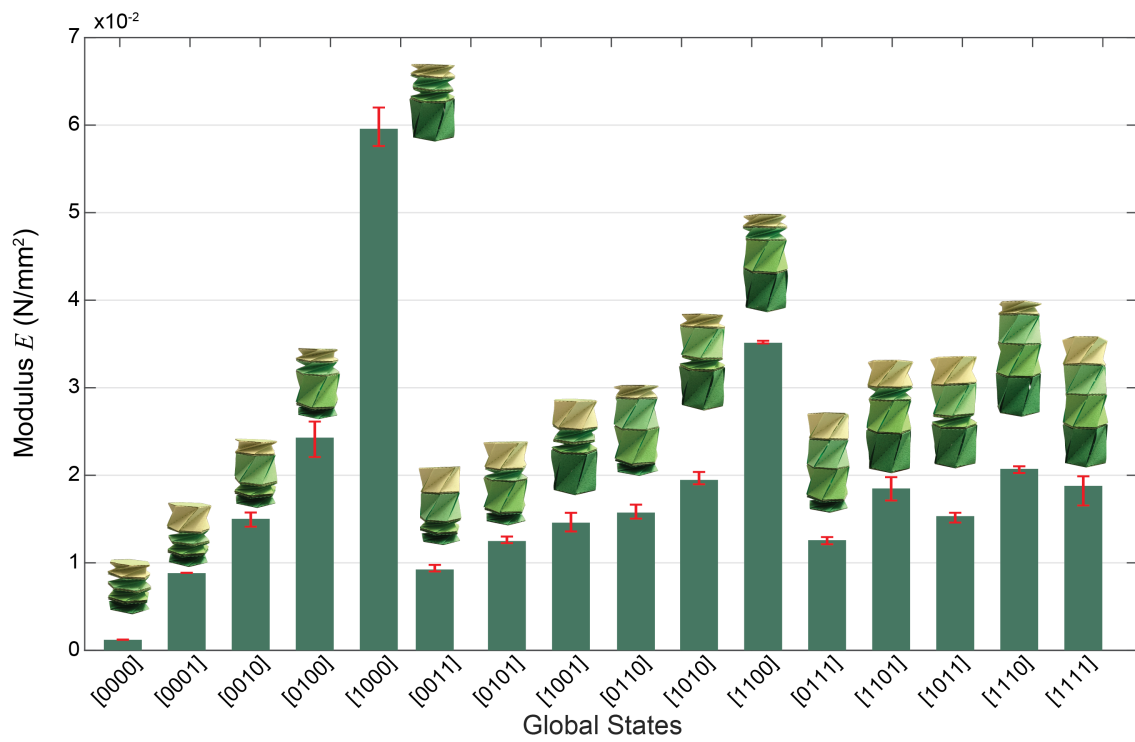


Fig. S8. Tunable mechanical response of the four-cell Kresling assembly. From multiple consecutive testing cycles, we obtain the average (columns) and maximum/minimum (error bars) values of the modulus E (Eq. S9)

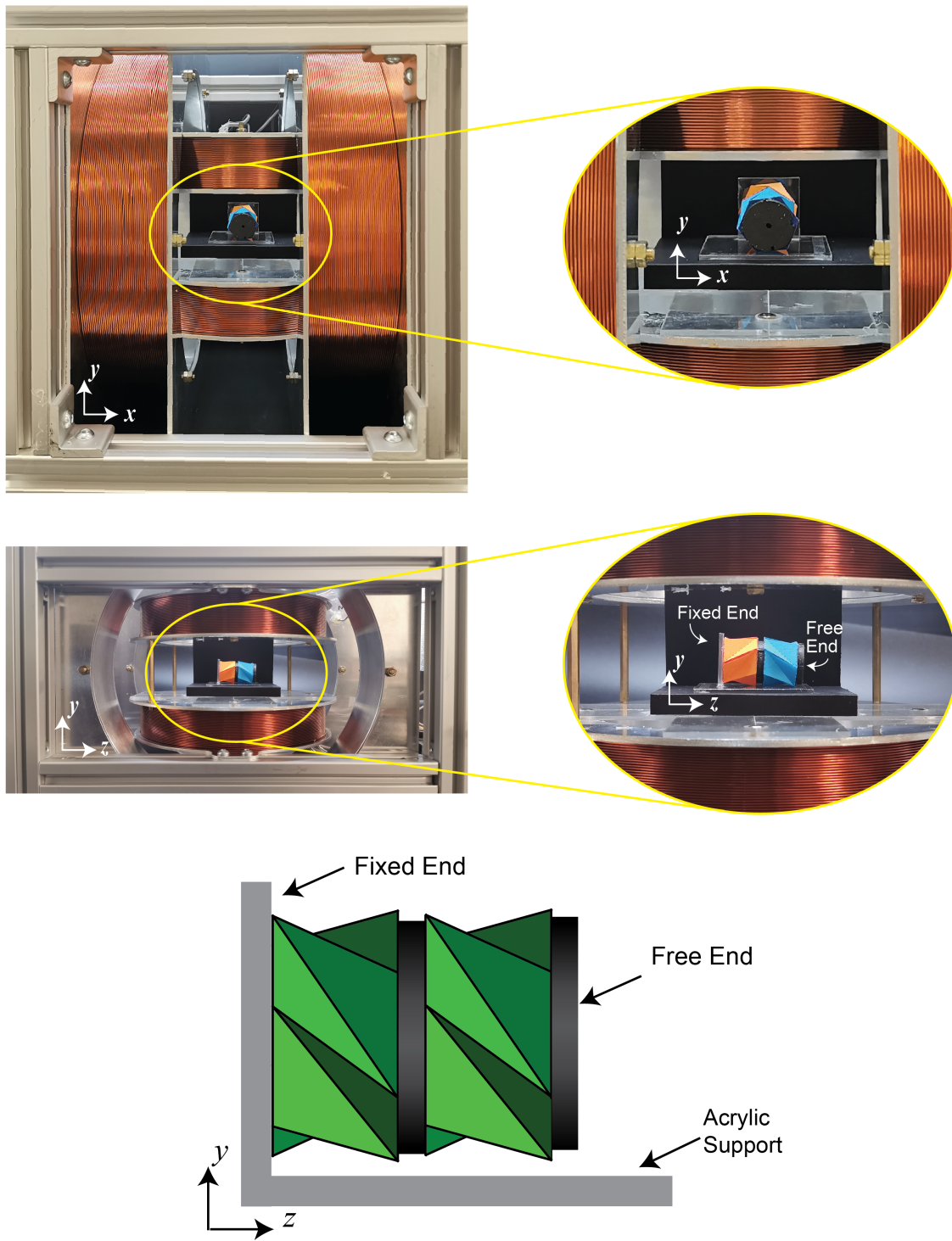


Fig. S9. Magnetic actuation setup with electromagnetic coils. Bottom schematic shows the boundary conditions of the sample inside the coils.

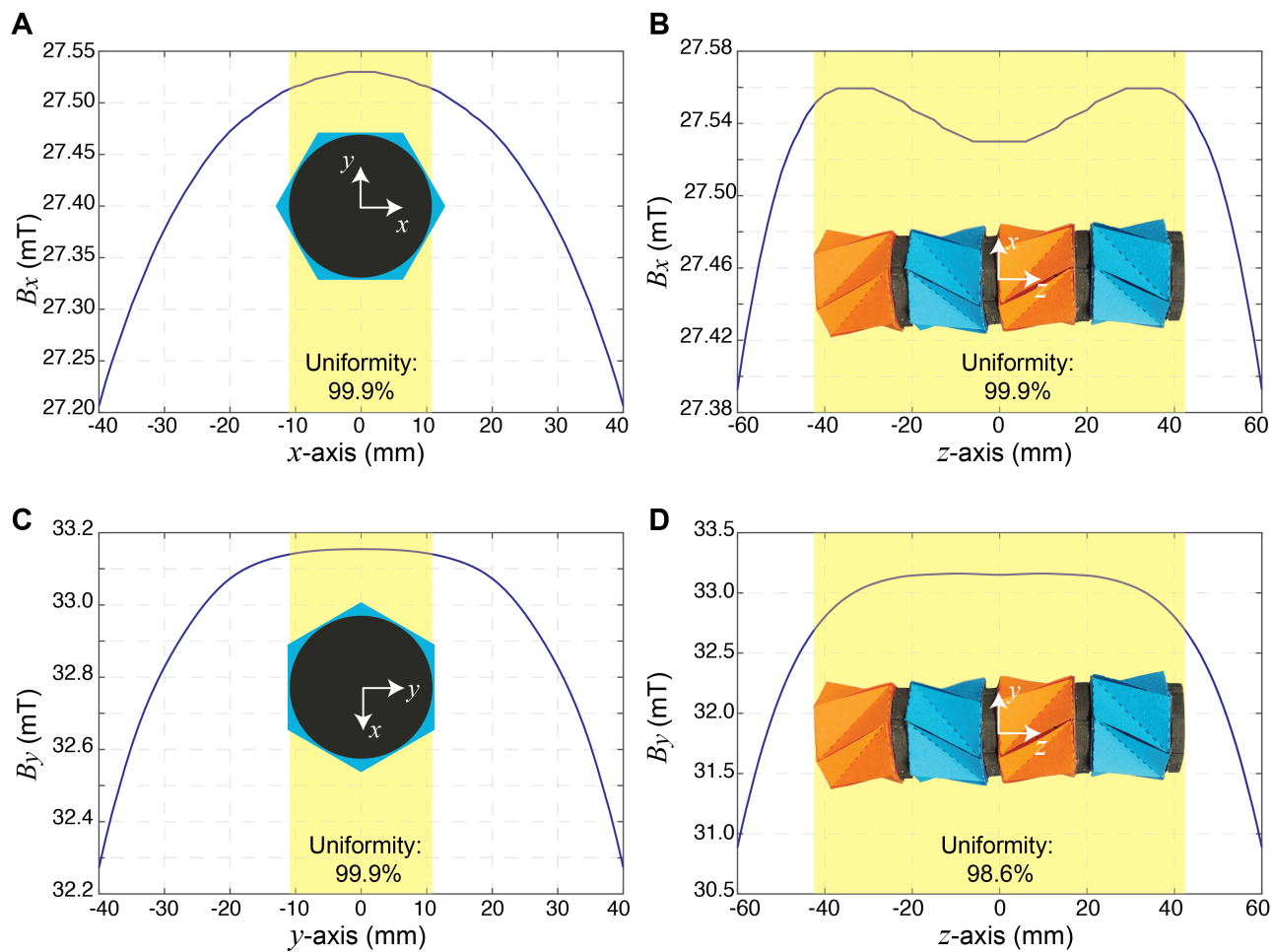


Fig. S10. The magnetic field distributions of 2D Helmholtz coils. (A) B_x along x axis. (B) B_x along z axis. (C) B_y along y axis. (D) B_y along z axis.

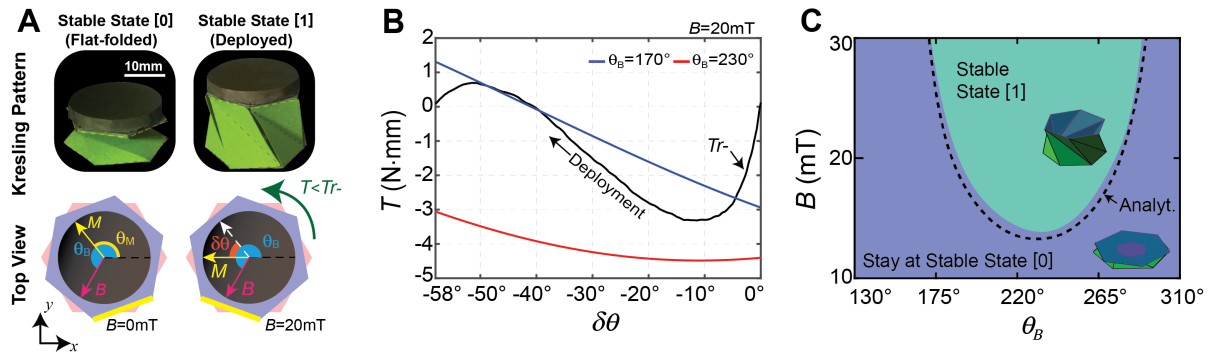


Fig. S11. Magnetic actuation of the Kresling pattern ($H = 18.2$ mm) from folded state [0] to deployed state [1] (A) Schematic of the actuation process, where $\theta_B = 240^\circ$ is the direction of the magnetic field \mathbf{B} , and the magnetization \mathbf{M} has direction $\theta_M = 129^\circ$. (B) Torque T_{r-} is required to switch the unit cell stable state, and the torques produced by the magnetic actuation versus the rotation angle $\delta\theta$ (C) Contour plot of the experimental and analytical (dashed lines) results for the deployment, showing if the unit cell will switch from stable state [0] to stable state [1], depending on the direction of the magnetic field θ_B and intensity of the magnetic field B .

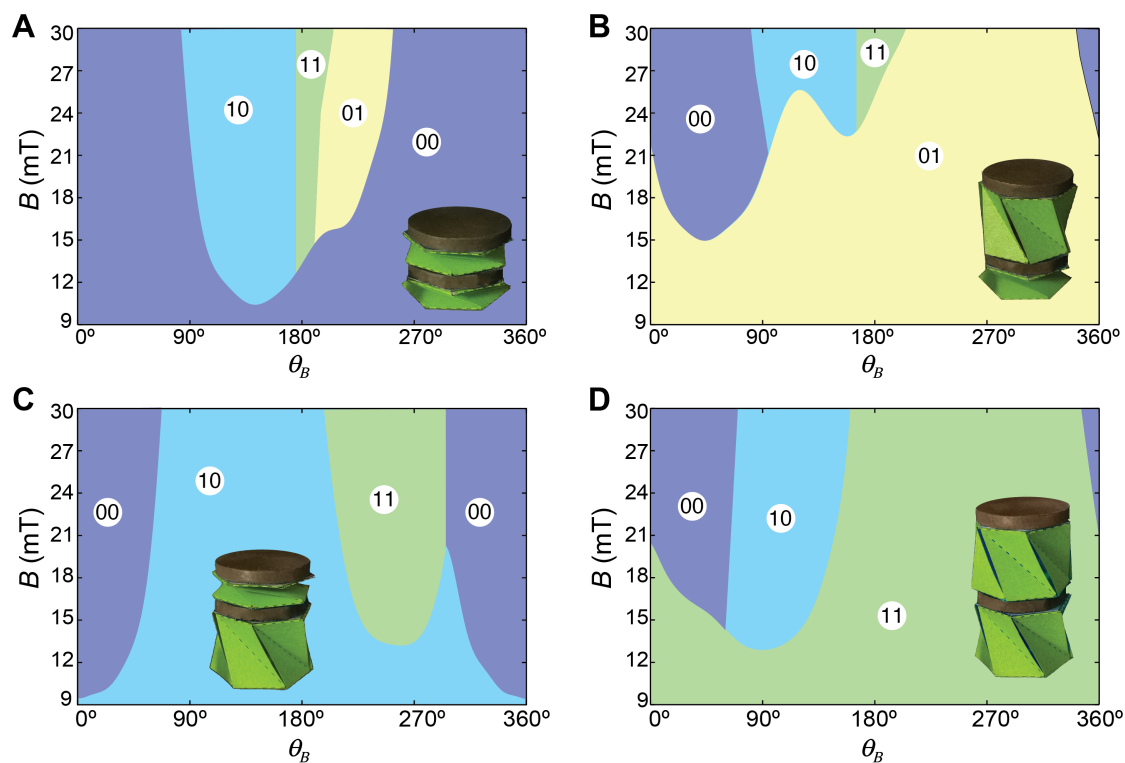


Fig. S12. Contour plots for the experimental measurements of the magnetic actuation of the two-cell Kresling pattern with same crease direction (Fig. 1). Actuation results from global (A) state [00], (B) state [01], (C) state [10], and (D) state [11].

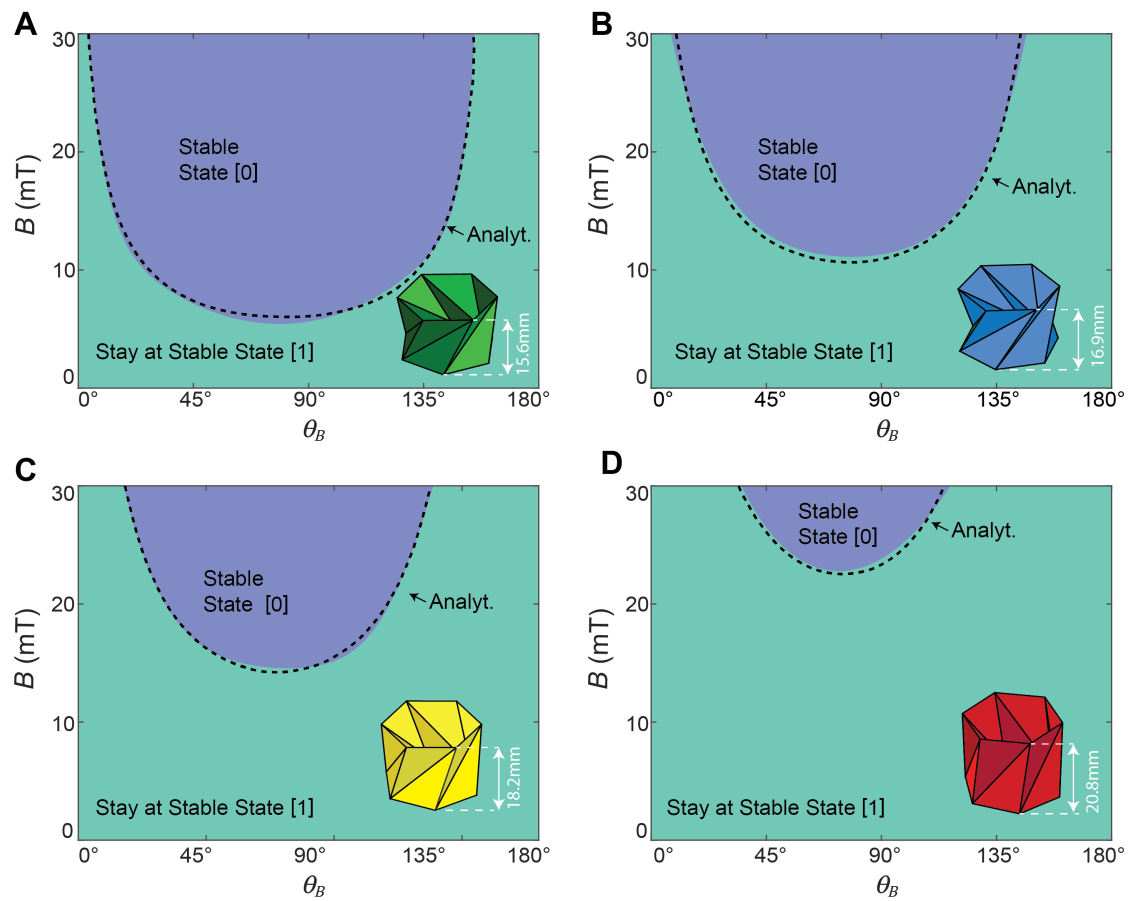


Fig. S13. Magnetic actuation contours for unit cells with geometries in Table S1. (A) Design 1 ($H_1 = 15.6$ mm). (B) Design 2 ($H_2 = 16.9$ mm). (C) Design 3 ($H_3 = 18.2$ mm). (D) Design 4 ($H_4 = 20.8$ mm).

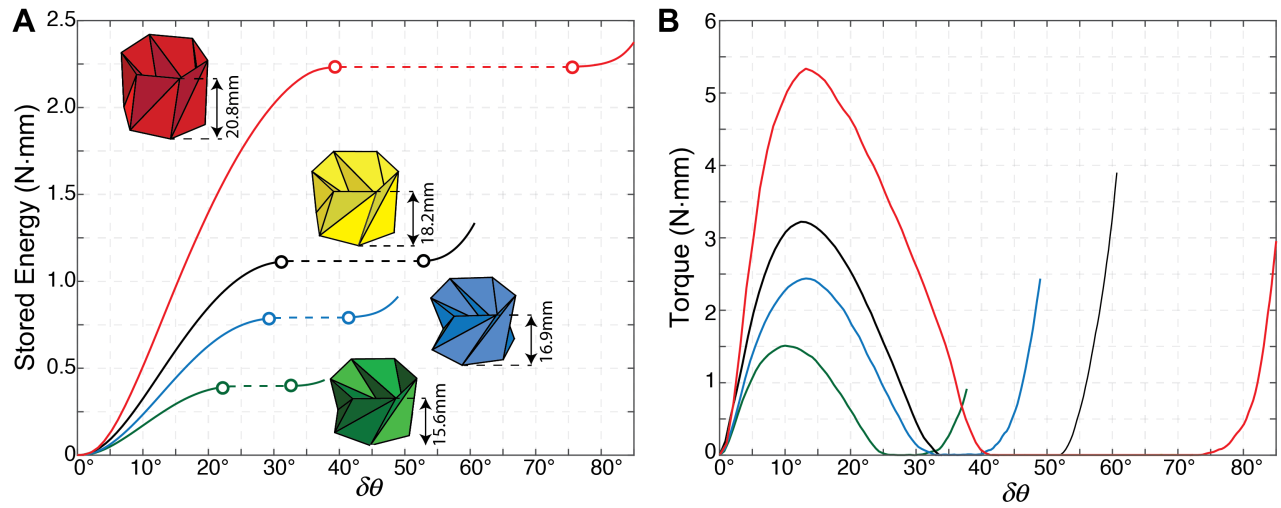


Fig. S14. Mechanical response obtained from the average of the force-displacement curves (Fig. 3A) of the unit cells tested with fixed-free boundary condition, i.e., setup #1 (Fig. S4). (A) Stored energy and (B) Torque required to fold each designed unit cell, where $\delta\theta$ is the rotation angle. Dashed lines represent the region in which the unit cell loses contact with the load cell.

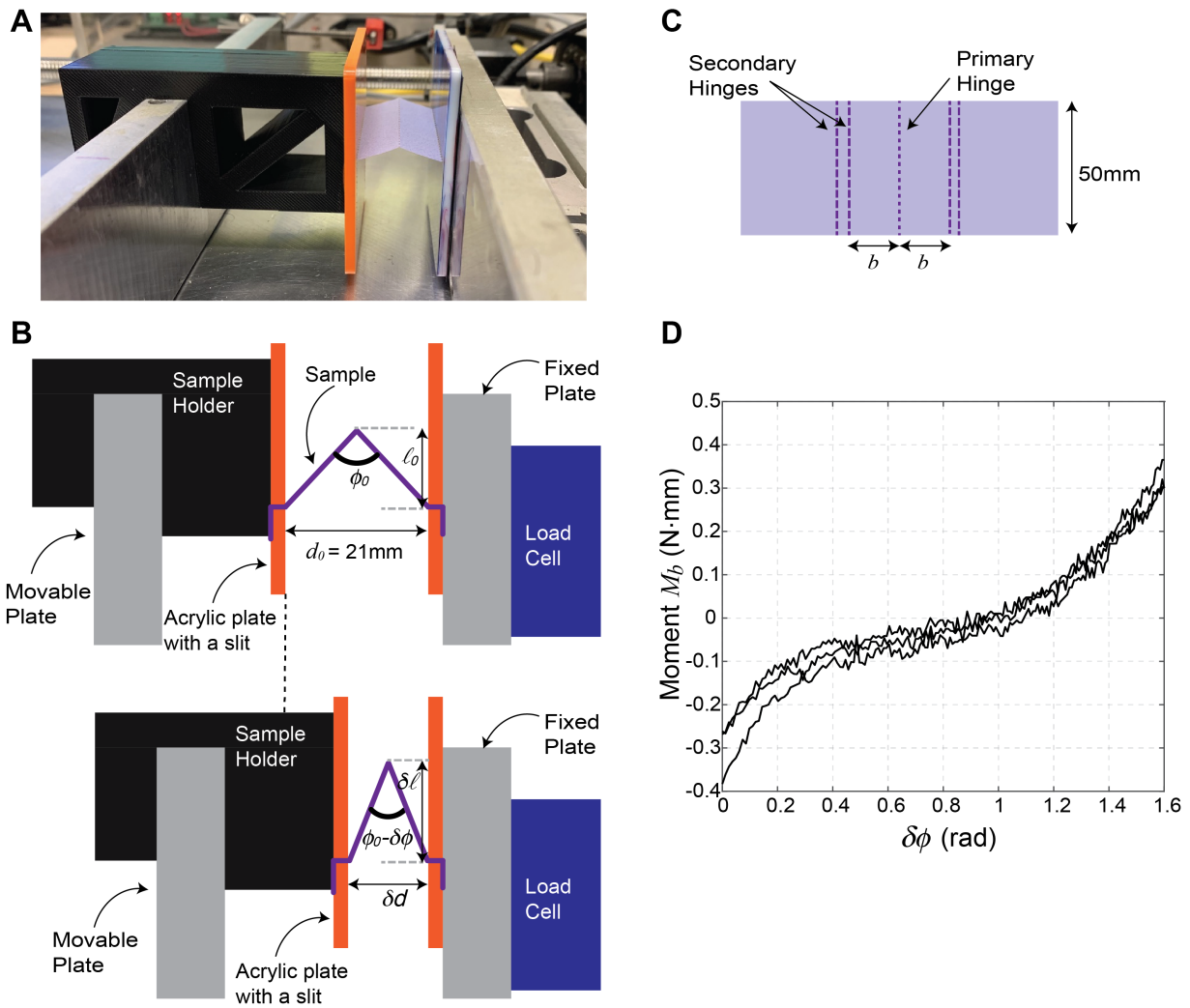


Fig. S15. Characterization of the rotational stiffness of the hinges. (A) Testing setup and (B) schematics. (C) Tested sample, where $b = 13\text{ mm}$. (D) Measured bending moment vs. rotation at the primary hinge, with each curve corresponding to one tested sample. From those curves, we obtain an average rotational stiffness $k_f = 2.4 \times 10^{-3}\text{ N}\cdot\text{mm}(\text{rad}\cdot\text{mm})^{-1}$

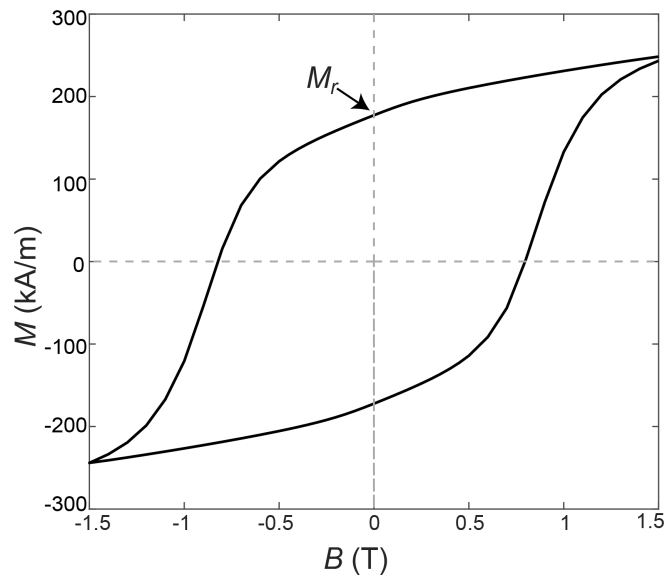


Fig. S16. The M-B curve of the magnetic material

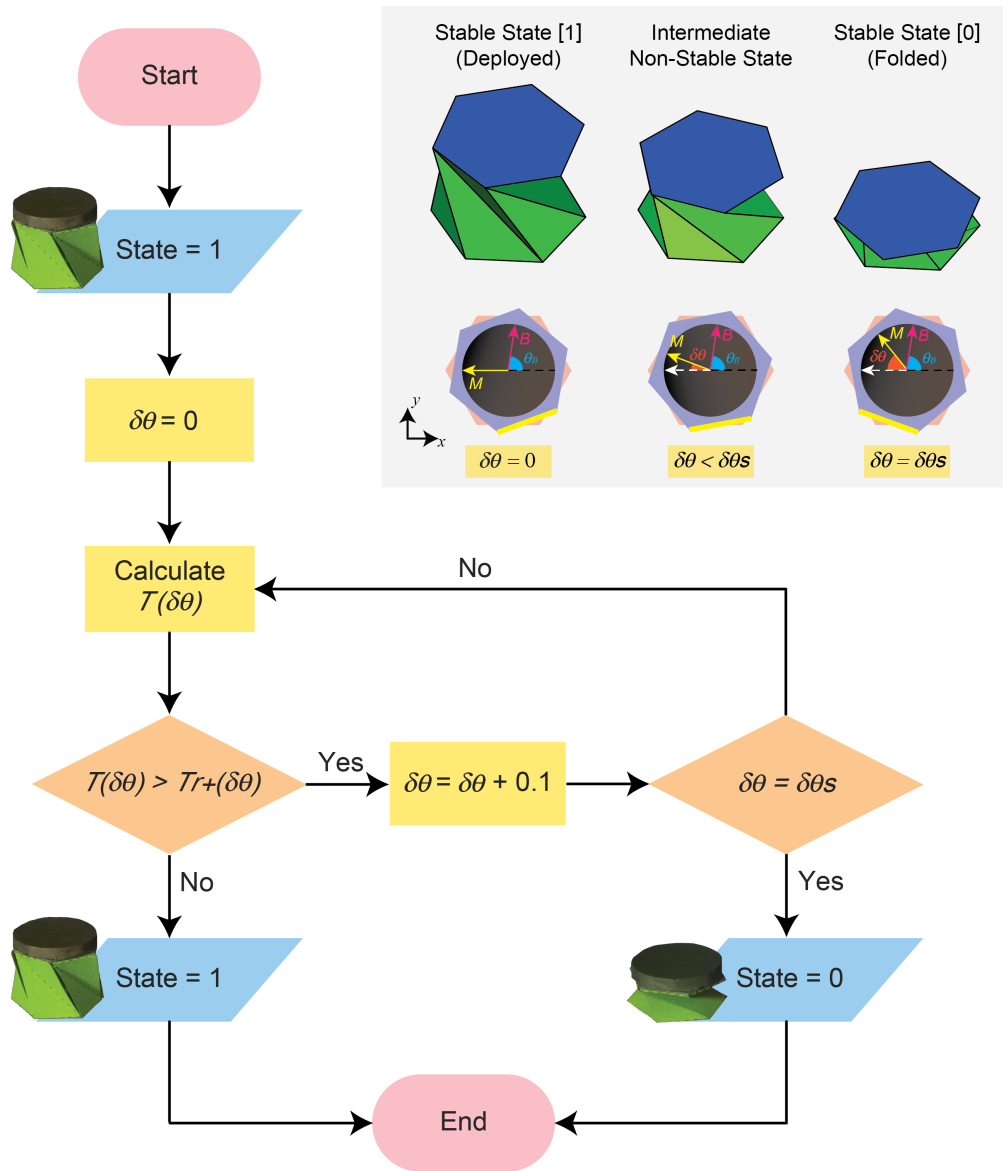


Fig. S17. Flowchart of the analytical calculation algorithm for the magnetic actuation of single unit cell with initial state [1]. Inset shows three different stages of the Kresling Pattern.

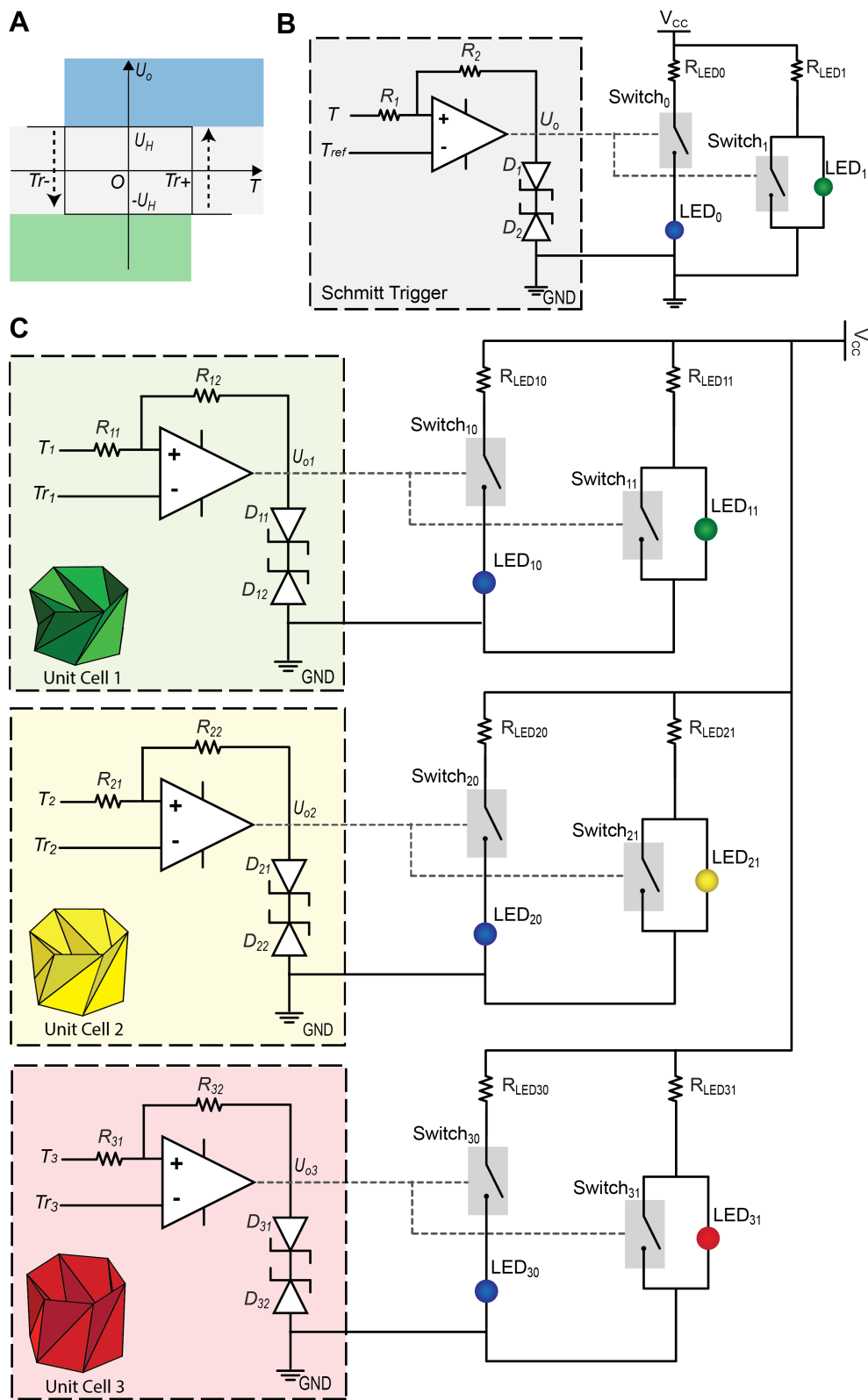


Fig. S18. (A) Hysteresis loop and (B) schematic of the Origami Schmitt Trigger for a Kresling unit cell. (C) Schematic of the LED demonstration for Kresling pattern assembly

Fast Origami Actuation: 0.2s

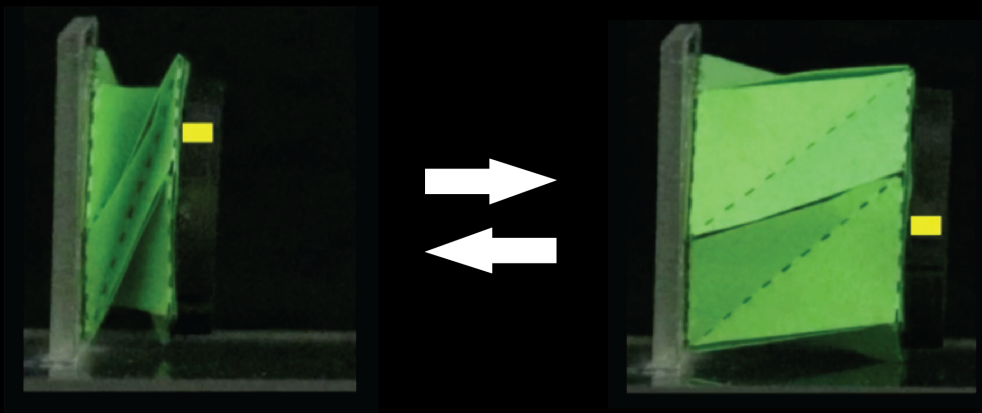


Fig. S19. Movie 1: Controlled origami actuation.

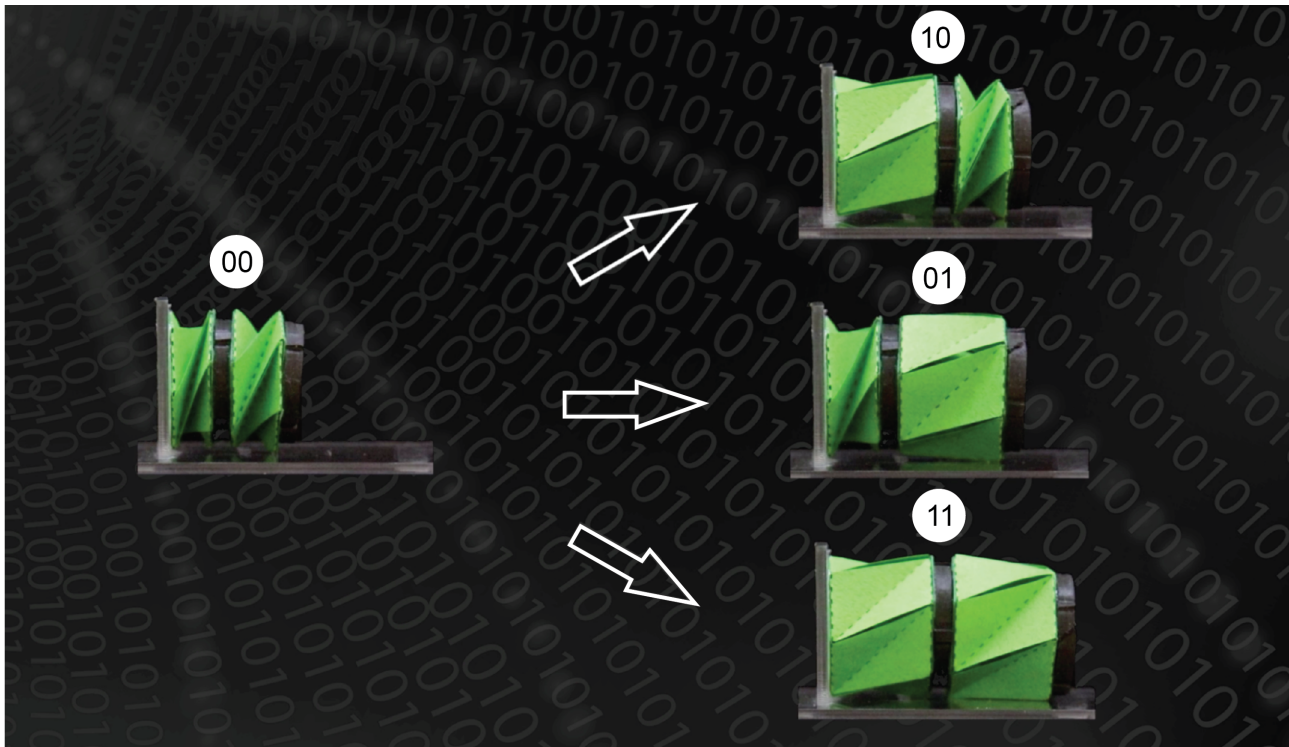


Fig. S20. Movie 2: Distributed actuation of a two-cell Kresling assembly.

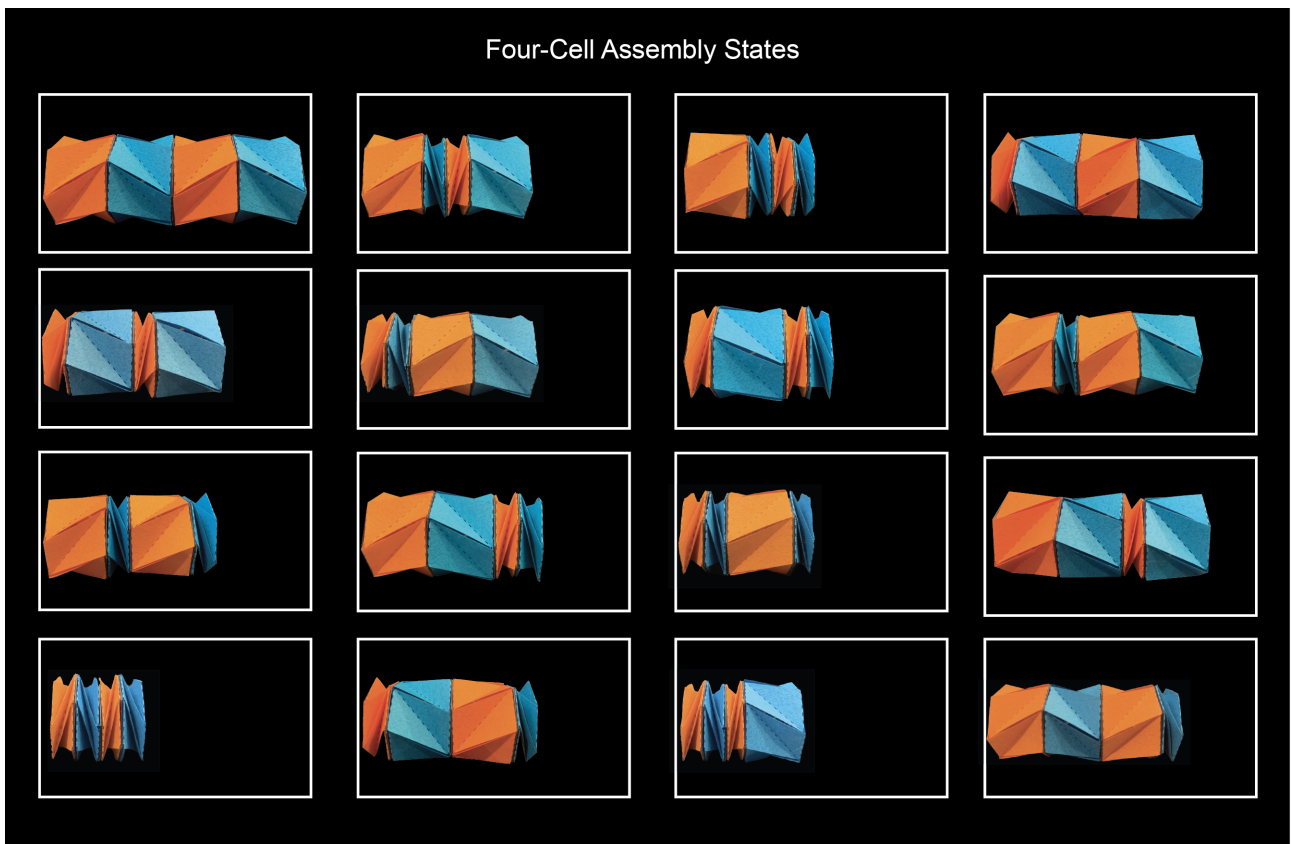


Fig. S21. Movie 3: Distributed actuation of Kresling assemblies with reverse creases

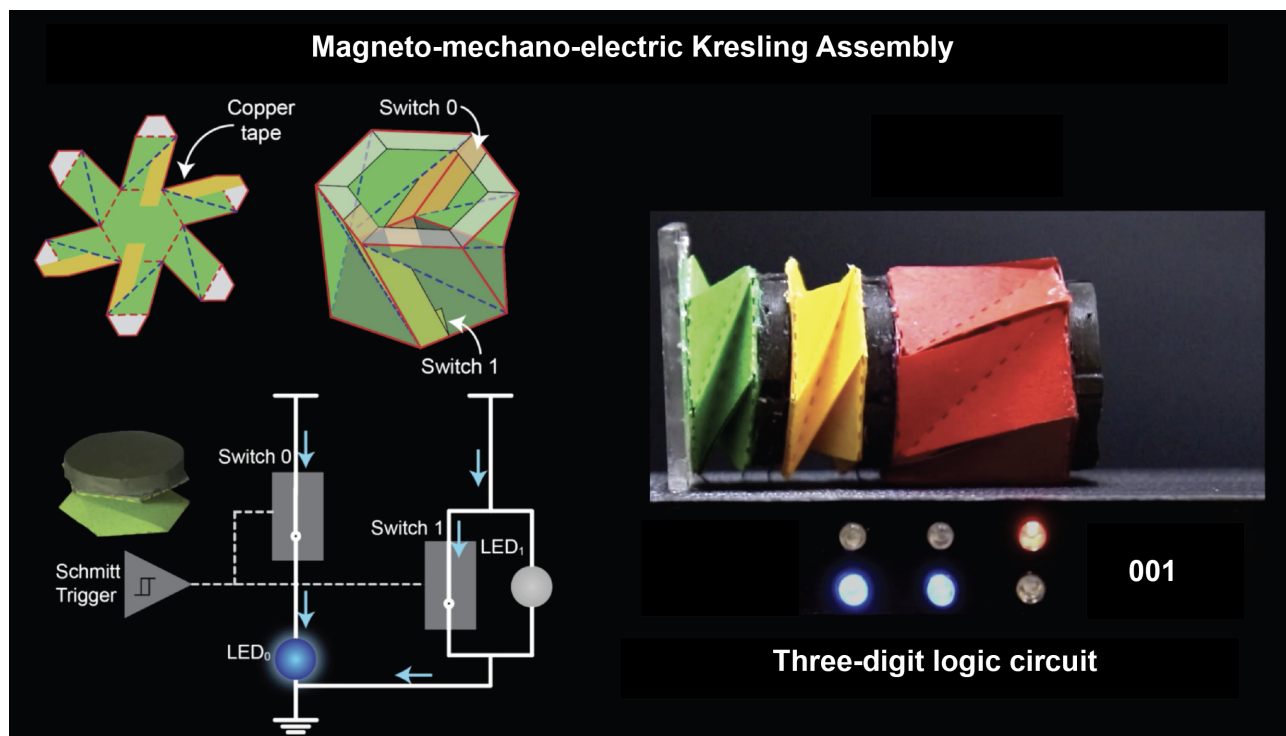


Fig. S22. Movie 4: Multifunctional Kresling assembly for digital computing

Table S1. Geometry of the Kresling Unit Cells

Design	H (mm)	α	c (mm)	a (mm)	ψ_1	ψ_2	$\Delta\psi$
1	15.6	107.72°	16.66	17.34	35.44°	84.56°	49.12°
2	16.9	105.40°	17.60	18.26	30.80°	89.20°	58.40°
3	18.2	102.77°	18.61	19.08	25.54°	94.46°	68.92°
4	20.8	96.18°	20.87	20.99	12.35°	107.65°	95.30°

Table S2. Unit cells design and actuation

Structure (Fixed to Free end)	Geometry	Magnetization direction Folded
Unit cell (Fig. 1A-C, Fig. S11)	Design 3	$\theta_M = 129^\circ$
Two-cell assembly (Fig. 1D-E, Fig. S12)	Design 3 (bottom)	$\theta_M = 0^\circ$
	Design 3 (top)	$\theta_M = 90^\circ$
Reversed creases assembly (Fig. 2)	Design 3 (orange)	$\theta_M = 0^\circ$
	Design 3 (blue)	$\theta_M = -90^\circ$
LED assembly (Fig. 4)	Design 1 (green)	$\theta_M = 0^\circ$
	Design 3 (yellow)	$\theta_M = 90^\circ$
	Design 4 (red)	$\theta_M = 180^\circ$

Movie S1. Controlled origami actuation.

Movie S2. Distributed actuation of a two-cell Kresling assembly.

Movie S3. Distributed actuation of Kresling assemblies with reverse creases.

Movie S4. Multifunctional Kresling assembly for digital computing.

References

1. B Kresling, Natural twist buckling in shells: from the hawkmoth's bellows to the deployable kresling-pattern and cylindrical Miura-ori in *Proceedings of the 6th International Conference on Computation of Shell and Spatial Structures*, eds. JF Abel, JR Cooke. pp. 1–4 (2008).
2. B Kresling, Folded tubes as compared to kikko (“Tortoise-Shell”) bamboo. *Origami3: Proc. Third Int. Meet. Origami Sci. Math. Educ.*, 197 (2002).
3. R.J. Lang, *Twists, tilings, and tessellations: Mathematical methods for geometric origami*. (CRC Press), (2017).
4. K Liu, GH Paulino, Nonlinear mechanics of non-rigid origami: an efficient computational approach. *Proc. Royal Soc. A: Math. Phys. Eng. Sci.* **473**, 20170348 (2017).
5. SE Leon, EN Lages, CN De Araújo, GH Paulino, On the effect of constraint parameters on the generalized displacement control method. *Mech. Res. Commun.* **56**, 123–129 (2014).
6. M Schenk, SD Guest, Geometry of Miura-folded metamaterials. *Proc. Natl. Acad. Sci.* **110**, 3276–3281 (2013).
7. E Filipov, K Liu, T Tachi, M Schenk, G Paulino, Bar and hinge models for scalable analysis of origami. *Int. J. Solids Struct.* **124**, 26–45 (2017).
8. N Nayakanti, SH Tawfick, AJ Hart, Twist-coupled kirigami cells and mechanisms. *Extrem. Mech. Lett.* **21**, 17–24 (2018).
9. K Liu, LS Novelino, P Gardoni, GH Paulino, Big influence of small random imperfections in origami-based metamaterials. *Proc. Royal Soc. A: Math. Phys. Eng. Sci.* (2020).